

Fuzzy Dark Matter Dynamics and the Quasi-Particle Hypothesis

Boris Zupancic*
(Dated: April 3, 2023)

Fuzzy Dark Matter provides an alternative wave description of cosmological dark matter. It behaves as a coherent Schrödinger wave with a characteristic wavelength of astrophysical scale. When in the presence of FDM, stellar material can be heated by dynamical processes very similar to the classical two-body relaxation. This suggests the *quasi-particle hypothesis*, which asserts that perturbations in FDM caused by wave interference behave like classical particles. Such an equivalence is useful as it allows one to refer to the extensive body of research in galactic dynamics when describing physical phenomena in FDM. We provide a fully self-consistent numerical approach to test this hypothesis, which has largely been avoided in the literature due to high computational costs. Our simulations are thus restricted to one dimension. Through two independent experiments, we find a one-to-one correspondence between perturbations in FDM, and their particle counterparts.

I. INTRODUCTION

Fuzzy Dark Matter (FDM) is an attractive alternative to the standard Λ -Cold Dark Matter (Λ CDM) model of cosmology. While Λ CDM is a highly successful theory on the large scales of the cosmos, issues arise on small scales as discrepancies between theoretical predictions and observation [1]. For example, cosmological numerical simulations of Λ CDM suggest large numbers of subhalos embedded in each dark matter halo; these would be satellite galaxies. In observation, we see far fewer satellite galaxies than otherwise predicted [2]. FDM resolves this problem of fine-structure by literally smoothing it out [3].

The fuzziness of FDM is an artifact of its theoretical foundations as a pseudo-scalar boson, or ultra-light scalar, a sector of dark matter that is well-studied and documented [4]. A particle with a light enough mass ($m \lesssim 30$ eV) can have a deBroglie wavelength that exceeds the interparticle separation of dark matter in space, and abundances of such particles subsequently behave as a coherent wave. Wave dark matter is thus a natural title for the general umbrella of such collections of ultra-light scalars; the FDM we are concerned with is specified by the boson mass range of $10^{-22}\text{eV} \leq m_{\text{FDM}} \leq 10^{-20}\text{eV}$, at which the deBroglie wavelength becomes astrophysical [5].

An interesting property of FDM arising from its wave nature is the ability to heat particles. In a dynamically active FDM halo, wave interference effects cause transient perturbations in the density profile, which in turn perturb the gravitational potential. Nearby stars will thus experience a change in velocity. Overall, a system of particles embedded within an FDM halo can experience a large increase in kinetic energy overtime. This phenomenon greatly resembles classical two-body relaxation [6]. In fact, there exists a hypothesis in the literature that asserts an equivalence between the naturally occurring perturbations in FDM and heavy particle systems; we refer to it as the *quasi-particle hypothesis*. A rigor-

ous treatment of FDM dynamical effects can be seen in [7], where they derive effective masses of FDM quasi-particles, and diffusion coefficients for both massless and massive particle cases. Formally, they suggest that the effective mass of an FDM quasi-particle is proportional to the local phase-space density.

The quasi-particle hypothesis and the associated dynamical heating effect have been used as an argument against the validity of FDM as a dark matter candidate. Through a Bayesian analysis of simulation data and observations of the Segue 1 and Segue 2 ultra-faint dwarf galaxies, Dalal & Kravtsov [8] infer a boson mass of $m \sim 10^{-19}\text{eV}$, outside the FDM mass range. However, their numerical techniques for simulation as described in [9], are not fully self-consistent. In particular, they assume that the FDM potential can be approximated as a static background with time-dependent first-order perturbations $\Phi(\mathbf{x}, t) = \Phi_0(\mathbf{x}) + \delta\Phi(\mathbf{x}, t)$. Moreover, the test particles used in [8] are massless.

Our goal is to perform a more numerically accurate test of the quasi-particle hypothesis, using fully self-consistent simulations that include both FDM and massive particles¹. We do so with two independent experiments. In the first, we compare the energy oscillations present in a purely N-Body simulation to those in a purely FDM simulation, while in the second, we directly compare the dynamical heating in a particle system of varying masses to that seen in a combined FDM and particle system. In both cases, we start from an equilibrium distribution. The end result is two separate accounts of the effective mass of a quasi-particle, which we hope to agree.

This paper is structured as follows: we first introduce the physical FDM and/or particle system in II, then describe the numerical scheme we followed and developed for integration in III; the two independent tests and their separate analysis follow in sections IV and V, before discussing the results and future directions in VI and VII.

* 18bz20@queensu.ca, boris.zupancic16@gmail.com

¹ Some of our animations can be seen by clicking this footnote.

II. THE SYSTEM

The governing set of equations for FDM is the Schrödinger-Poisson system [3],[4],[5],[10],[11]:

$$\begin{cases} i\hbar \frac{d\psi}{dt} = -\frac{\hbar^2}{2m} \nabla^2 \psi + m\Phi\psi \\ \nabla^2 \Phi = 4\pi G \rho \\ \rho \equiv m|\psi|^2 \end{cases} \quad (1)$$

where \hbar is the reduced Planck's constant, G is Newton's constant, Φ is the gravitational potential, and ψ is the FDM wavefunction. Further ρ is the mass density that produces Φ , and m is the FDM boson mass. The wavefunction is *not* quantum mechanical, but rather represents the number density of bosons when norm-squared; this is the meaning of the third equation in the system (1). Note that in the case of periodic boundary conditions, such as in a cosmological simulation, the Jeans' Swindle [6] replaces the mass density with the perturbation from the mean: $\rho = m(|\psi|^2 - \langle |\psi|^2 \rangle)$.

The force on a particle in a gravitational potential is described by Newton's 2nd Law:

$$\frac{d^2 \mathbf{x}}{dt^2} = -\nabla \Phi(\mathbf{x}) \quad (2)$$

Thus the combined FDM-Particle system is described by both sets of equations upon replacement of the mass density by:

$$\rho \equiv \rho_{\text{FDM}} + \rho_{\text{part}} \quad (3)$$

Here ρ_{FDM} is the mass density of FDM as described above, while ρ_{part} is the density given by the spatial distribution of particles; it may be written as the sum of Dirac delta functions:

$$\rho_{\text{part}}(\mathbf{x}) = \sum_{i=1}^{N_{\text{part}}} m_i \delta(\mathbf{x} - \mathbf{x}_i) \quad (4)$$

where m_i is the mass of the i -th particle, and \mathbf{x}_i its position. In practice, this is computed using histograms (see appendix A).

For ease of describing the numerical techniques in Section III, and remaining consistent with the approach in our code, we non-dimensionalize the above equations by making the substitutions:

$$\begin{cases} \Phi \mapsto v_s^2 \Phi \\ \psi \mapsto L_s^{-3/2} \psi \\ x \mapsto L_s x \\ t \mapsto T_s t \\ m_{\text{FDM}} \mapsto M_s m_{\text{FDM}} \end{cases} \quad (5)$$

where v_s , L_s , are velocity and length scales respectively, $T_s \equiv \frac{L_s}{v_s}$ is the corresponding time scale, and M_s is the

mass scale, retrieved by setting Newton's constant to unity $G = 1$:

$$[G] = M_s^{-1} L_s^3 T_s^{-2} \Rightarrow M_s \equiv \frac{L_s^3}{T_s^2} = v_s^2 L_s \quad (6)$$

We further introduce a *fuzziness parameter*:

$$r \equiv \frac{\hbar}{2m_{\text{FDM}} v_s L_s} \mapsto \frac{\hbar}{2m_{\text{FDM}}} \quad (7)$$

where the second part is r after being non-dimensionalized.

The full (dimensionless) system of equations for the FDM-Particle system is thus:

$$\begin{cases} i \frac{\partial \psi}{\partial t} = -r \nabla^2 \psi + \frac{1}{2r} \Phi \psi \\ \frac{d^2 \mathbf{x}_i}{dt^2} = -\nabla \Phi(\mathbf{x}_i) \\ \nabla^2 \Phi = 4\pi (\rho_{\text{FDM}} + \rho_{\text{part}}) \end{cases} \quad (8)$$

where the index i ranges over all particles.

III. NUMERICAL TECHNIQUES

Our simulations come with a caveat: in order to cut back on computational costs, we reduce system (8) to 1D by making the replacements:

$$\mathbf{x} \mapsto x \quad \text{and} \quad \nabla^2 \mapsto \frac{\partial^2}{\partial x^2} \quad (9)$$

In this section we will describe the full numerical scheme of our simulations, a modified particle-mesh code [12] that fully self-consistently evolves the mixed particle and FDM system. It can be divided into 4 main components: the setup of the initial conditions III A, numerical integration of the Poisson equation III B, numerical integration of the Schrodinger equation III C, and the visualization of the FDM component through the Husimi transform III D.

Although the last of these is merely a visualization, there are important implications for how fine one must make the numerical grid on which the system lives.

Many technical details are left to the appendix A, along with other capabilities of the developed code (such as the ability to evolve the system under periodic boundary conditions).

A. Initial Conditions

For the particles, given a phase-space distribution, the profile can be sampled using the accept/reject method [13].

For FDM, we use a trick from Widrow&Kaiser [11] to turn the distribution function into a wavefunction:

$$\psi(x_n) = \frac{1}{\sqrt{N m_{\text{FDM}}}} \sum_{k=0}^{N-1} \sqrt{f(x_n, v_k)} R_k e^{ip_k x_n} \quad (10)$$

where f is the chosen distribution, x_n is the n -th point on our numerical grid, N is the number of grid points, $\{v_k\}_{k=0}^{N-1}$ is the sampled sequence of velocities, $p_k = m_{\text{FDM}} v_k$, and $\{R_k = e^{i\theta_k}\}_{k=0}^{N-1}$ is a random sample of N complex numbers, uniformly distributed on the unit circle.

1. Lowered Spitzer ICs

In our simulations, we choose initial conditions from an equilibrium distribution that we call the lowered Spitzer model. It is obtained by truncation of the ordinary Spitzer model, used to describe the vertical structure of a thin axis-symmetric disk (see [6, Q4.21]):

$$f(x, v_x) = \begin{cases} f_0(e^{-(E_x - E_0)/\sigma_x^2} - 1) & , 0 \leq E_x \leq E_0 \\ 0 & , \text{otherwise} \end{cases} \quad (11)$$

where $f_0 = \frac{\rho_0}{\sqrt{2\pi}\sigma_x^2}$, and $E_x = \frac{1}{2}v_x^2 + \Phi(x)^2$. The other variables, ρ_0 , E_0 and σ_x are all control parameters, representing the mean density, truncation/maximum energy, and velocity dispersion, respectively. In all the simulations displayed in the following sections, we chose $f_0 = 0.1$, $E_0 = 0.7$ and $\sigma_x = 0.5$, yielding a total mass of $M \approx 0.466$.

As this distribution function has a dependence on the gravitational potential Φ , it is coupled to Poisson's Equation. In our simulations, we require a full solution of the distribution dependent only on position and velocity x, v_x , so that we may instantiate ψ on the numerical grid. In this case, the density can be determined in terms of the standard error function [14]:

$$\rho(\Phi(x)) := \int_{-\infty}^{\infty} f(x, v_x) dv_x \quad (12)$$

$$= 2^{3/2} f_0 \sigma \left(\frac{\pi^{1/2}}{2} e^{t_m^2} \text{erf}\{t_m\} - t_m \right) \quad (13)$$

where $t_m = (E_0 - \Phi(x))^{1/2}/\sigma_x$. In our code, we numerically solve Poisson's equation using Runge-Kutta 4 [15] to obtain density and potential profiles for the lowered Spitzer model when instantiating our physical system.

However, throughout the time-evolution component of the code, we compute the potential using a different algorithm.

B. Isolated Poisson Solver

To solve for Φ under isolated boundary conditions, we use a trick from Hockney&Eastwood [12]. This is a similar approach to the periodic case (see appendix A), except we are turning the Green's function convolution:

$$\frac{d^2\Phi}{dx^2} = 4\pi\rho \iff \Phi(x) = 4\pi \int G(x - x')\rho(x')dx' \quad (14)$$

into a discrete fourier analysis problem:

$$\Phi(x) = \frac{2L}{2N-1} \sum_{k=0}^{2N-2} \hat{G}_k \hat{\rho}_k e^{ikx} \quad (15)$$

and further performing this calculation over the doubled numerical grid ($2N - 1$ points), with the density set to zero on the extended portion $\rho_n = 0$ for all $n > N - 1$. Note that above, \hat{G}_k and $\hat{\rho}_k$ denote Fourier coefficients (obtained using the fast fourier transform (FFT)).

As discussed in [16], this method does not simply suppress the periodicity given by the FFT for the points n where $\rho_n \neq 0$, but gives the correct solution for isolated boundary conditions.

Relating to our code, the Green's function for the 1D Laplacian $\nabla = \frac{\partial^2}{\partial x^2}$ is

$$G(x) = \frac{1}{2}|x| \quad (16)$$

C. Time Evolution

The numerical time-integration of system (8) is the main component of the code that develops the physics. Given a wavefunction ψ instantiated on the numerical grid and/or a system of particles, as described in III A, we push the system forward in time using a *Kick-Drift-Kick* algorithm adapted from [3],[10].

Half of this algorithm is devoted to the FDM, in integrating the Schrödinger Equation:

$$\psi(t + \Delta t, x) = \left[\mathcal{T} \circ e^{-i \int_t^{t+\Delta t} (-r\partial_x^2 + \frac{1}{2r}\Phi(t,x))} \right] \cdot \psi(t, x) \quad (17)$$

$$\approx \left[e^{-i \frac{\Delta t}{4r}\Phi(t+\Delta t, x)} \circ e^{ir\Delta t\partial_x^2} \circ e^{-i \frac{\Delta t}{4r}\Phi(t, x)} \right] \cdot \psi(t, x) \quad (18)$$

$$= \left[\underbrace{e^{-i \frac{\Delta t}{4r}\Phi(t+\Delta t, x)}}_{\text{Kick 2}} \circ \underbrace{\text{FFT}^{-1} \circ e^{ir\Delta tk^2} \circ \text{FFT}}_{\text{Drift}} \circ \underbrace{e^{-i \frac{\Delta t}{4r}\Phi(t, x)}}_{\text{Kick 1}} \right] \cdot \psi(t, x) \quad (19)$$

Here \mathcal{T} denotes the time-ordering operator. The three

pieces of the algorithm can be seen in the last line. Note

that between *Drift* and *Kick 2*, it is necessary to update the potential.

As our simulations are meant to be fully self-consistent, we must carry out essentially the same steps in time evolution of the particle portion of the system. Thus, the second half of the algorithm has steps:

$$\text{KICK 1: } v(t + \Delta t/2) = v(t) + a(t) \frac{\Delta t}{2} \quad (20)$$

$$\text{DRIFT: } x(t + \Delta t) = x(t) + \Delta t \cdot v(t + \Delta t/2) \quad (21)$$

$$\text{Update } \Phi. \text{ (Get } a(t + \frac{1}{2}\Delta t) = -\partial_x \Phi(t + \frac{1}{2}\Delta t)) \quad (22)$$

$$\text{KICK 2: } v(t + \Delta t) = v(t + \Delta t/2) + \frac{\Delta t}{2} a(t + \Delta t/2) \quad (23)$$

When simulating the full system comprised of both FDM and particles, the corresponding steps are carried out at the same time, to preserve the order of *Kick-Drift-Kick*.

Another technicality to consider is the Courant condition [17]. For our explicit time-integration, we require that the time-step does not exceed the minimal time to cross a grid cell of length Δx :

$$\Delta t \leq \frac{\Delta x}{v_{\max}} \quad (24)$$

Here we take the denominator to be the maximal speed present in the system, which exists and is $v_{\max} = \sqrt{2E_0}$ given our equilibrium ICs. The requisite mesh-size Δx is determined below.

In the appendix A 5, we find that the computational complexity of this algorithm, for the FDM component only, goes like:

$$N(5 + 4 \log 2) + 6N \log(N) \quad (25)$$

D. The Husimi Transform

Obtaining a visual representation of the physical system is necessary to make qualitative observations. In both cases, particles or FDM, it is simple to plot the approximate density on the grid. Obtaining the phase-space distribution for particles is also straight-forward: on a 2D-plane, scatter-plot x and v for each particle.

Visualizing FDM in phase-space, on the other hand, requires use of the Husimi-Q transform [11]. This is a (gaussian) windowed-fourier transform that gives a limited-resolution representation of the wavefunction in both position and momentum:

$$\begin{aligned} \Psi(x, p) = & \left(\frac{1}{2\pi\hbar} \right)^{1/2} \left(\frac{1}{\pi\eta^2} \right)^{1/4} \\ & \times \sum_{k=0}^{N-1} e^{-(x_k - x)^2 / 2\eta^2} e^{-ip(x_k - x/2)/\hbar} \psi(x_k) \end{aligned} \quad (26)$$

Here η is the width of the Gaussian window, and N is the number of grid points. In our code, and for the system

(8), $\hbar = 1$. Further, the momentum representation at a fixed point $\varphi_x(p)$ is calculated using an FFT, which determines coefficients only up to a maximum frequency $k_{\max} = \frac{p_{\max}}{\hbar} \cong \frac{2\pi}{L} \frac{N}{2} = \frac{\pi N}{L}$, where L is the length of the numerical box. This brings some technicalities into consideration.

1. Mesh-Size and Resolution

We have two issues to consider regarding Eq(26):

1. The required mesh-spacing Δx , or equivalently number of grid points N , such that the entire system in phase-space is covered by the FFT.
2. The optimal η for which we obtain equal resolution in both x and p .

The first issue references that if the maximal momentum attainable by the FFT is less than the maximum momentum present in the system (which exists in the lowered Spitzer model), then the Husimi transform fails to compute a full phase-space representation. Solving this issue is not just important for visualization, but also for the reliability of the algorithms described in this section, which are dependant on the FFT.

This is solved by demanding that the maximum velocity represented in the FFT and the maximum velocity in our ICs are equal. In the lowered Spitzer model, there is a truncation length $x_t = \Phi^{-1}(E)$ and truncation velocity $v_t = \sqrt{2E_0}$. We set-up the discretized distribution function $f(x, v)$ over a position-velocity box of dimensions $[L, V] = [2\alpha x_t, 2\beta v_t]$, for some $\alpha, \beta \in \mathbb{R}_{>1}$. While L remains fixed throughout the simulation as the length of our numerical grid, the range in velocity V is only constructed for the ICs, to be summed over in Eq(10). During the simulation, our FFTs must cover the original velocity range V ; that is, we demand:

$$2v_{\max} = 2\beta v_t \Leftrightarrow \frac{\pi\hbar N}{mL} = \beta v_t \quad (27)$$

This yields two equivalent conditions for our numerical grid:

$$N = \frac{\alpha\beta}{\pi} \frac{x_t v_t}{r} \quad (28)$$

$$\Delta x = \frac{\pi\hbar}{m\beta v_t} \quad (29)$$

where in the first equation we have used that $r = \hbar/2m$. If N is smaller than the above, or equivalently if Δx is larger than the above, the FFT (and thus Husimi, algorithms, etc) fails to cover the whole range of velocities present in the system. Note that this heightens the computational complexity, as a smaller fuzziness r increases the number of grid points N . Further, the Courant condition will imply a shorter time-step with smaller r , meaning longer CPU time.

The second issue on resolution is solved noting that resolution in position x goes as η , while resolution in frequency k goes as $1/\eta$. Assuming the same box dimensions L, V as before, the number of resolution elements in x and v are:

$$\#x \text{ elements} = \frac{L}{\eta} = \frac{2\alpha x_t}{\eta} \quad (30)$$

$$\#v \text{ elements} = \frac{V \frac{\hbar}{m}}{1/\eta} = \frac{2\beta v_t \hbar \eta}{m} \quad (31)$$

where we have used the fact that the number of v elements is exactly the number of frequency elements.

Setting these equal:

$$\frac{\alpha x_t}{\eta} = \frac{\beta v_t \hbar \eta}{m} \quad (32)$$

$$\Rightarrow \eta = \left(\frac{\alpha x_t}{\beta v_t} \right)^{1/2} \sqrt{\frac{2}{r}} \quad (33)$$

meaning the resolution scales as $\eta \sim \sqrt{N}$.

IV. ENERGY OSCILLATIONS

Oscillations in Kinetic and Potential Energy naturally arise in N-body systems through the discrete approximation of a smooth equilibrium model. A comprehensive analysis of the phenomenon can be seen in [18]. As FDM is represented by a continuum, one may not expect to see energy oscillations at all. However, Eq(10) implies that the numerical setup of an FDM wavefunction is such that $\rho_{\text{FDM}} = m|\psi|^2$ naturally deviates from the true distribution. The perturbations in ρ_{FDM} are our *quasi-particles*, and we expect them to cause the same energy oscillations as seen in N-body simulations. This argument serves as a basis for the quasi-particle hypothesis.

Moreover, as the true distribution for FDM is only realized in the limit of an infinitely fine mesh, we should see the amplitude of oscillations decrease with a decrease in the deBroglie wavelength, or equivalently the fuzziness r (recall the relation to mesh-size argued in IIID). This mirrors the fact that energy oscillations in N-body simulations decrease with a higher particle number, equivalent to a finer discretization.

Our goal in this section is to test the hypothesis by simulating two regimes: pure particles and pure FDM. With a simple empirical analysis of the oscillations corresponding to varying particle numbers and fuzziness parameters, we arrive at an inverse power law for the effective number of quasi-particles in the FDM, seen below in Eq(36).

A. Pure Particles

We run numerous simulations for numbers of particles ranging between 10^2 and 10^5 , with the lowered

Spitzer equilibrium model as the IC, for 256 collapse times ($t_{\text{collapse}} = z_{\text{rms}}/v_{\text{rms}}$, approx 0.25 in our case).

In Figure 1 can be seen a typical example of a simulation, with 30000 particles. We see how the energies (kinetic, potential, total) vary from the mean with time, along with the behaviour of the ratio of kinetic to potential energy $K/|W|$. The system behaves as expected, with a clear beat pattern in the energies, and maintains approximate equilibrium, with $K/|W|$ oscillating around a mean of $1/2$, equal to the virial ratio. Note it is somewhat non-trivial to show that the virial ratio for 1D gravity is in fact $1/2$, which we elaborate on in appendix B.

In Figure 3 we plot the power spectrum for oscillations in the kinetic energy. There is a clear structure, with three visually discernible peaks; a rough estimate is around $\sqrt[3]{k} \approx 2$, $\sqrt[3]{k} \approx 2.5$, and a third at $2.5 < \sqrt[3]{k} < 3$. We find that the values of these fundamental frequencies do not greatly change over the range of simulations.

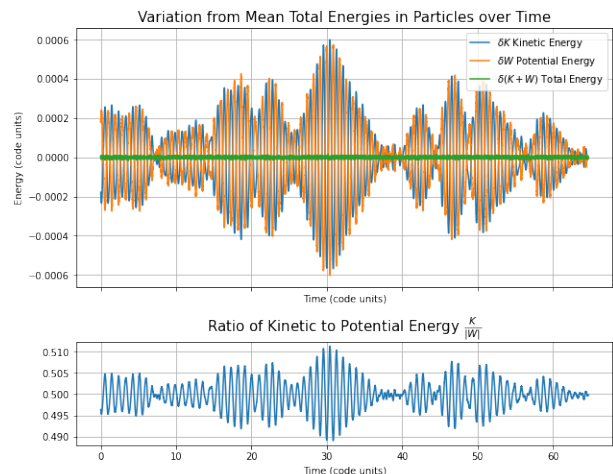


FIG. 1: (Top) The variation from the mean for Kinetic, Potential, and total Energies in a 30000 particle system, over 256 collapse times. (Bottom) The ratio $K/|W|$, hovering around $1/2$.

B. Pure FDM

Here we display the corresponding plots for the FDM scenario, for an example simulation of 256 collapse times and a fuzziness parameter $r \approx 0.00099$. The energies + ratio and power spectrum are seen in Figures 2 and 3, respectively. There is little to no qualitative visual difference with the N-body case. The oscillatory behaviour is essentially the exact same, with the power spectrum being nearly identical.

C. Correspondence

Beyond the clear similarity of the waveforms seen above, it is possible to draw an empirical one-to-one

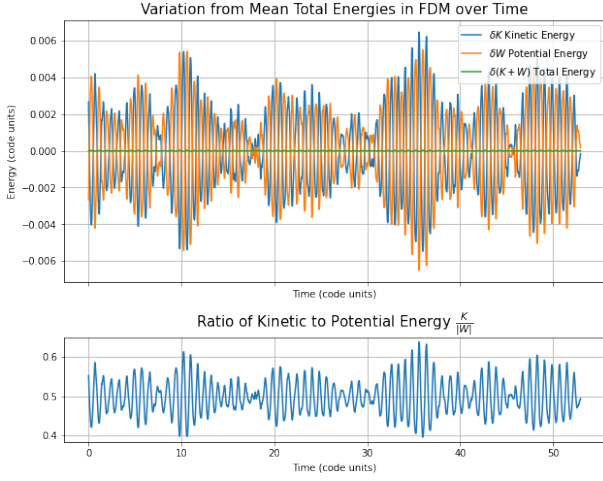


FIG. 2: (Top) The variation from the mean for Kinetic, Potential, and total Energies in an FDM system with $r = 0.0009904843310491913$, over 256 collapse times. (Bottom) The ratio $K/|W|$, hovering around $1/2$.

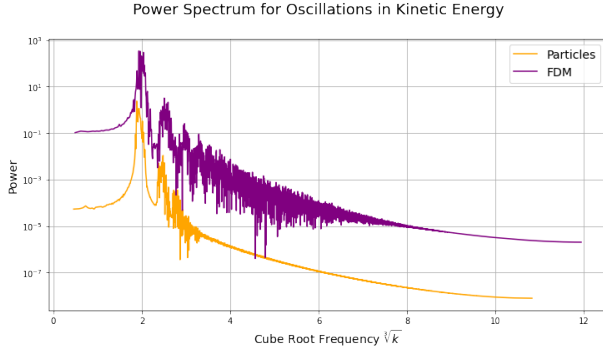


FIG. 3: The power spectra for the oscillations seen in Figures 1 and 2. Orange corresponds to the particles, and purple to the FDM.

correspondence between the number of particles N and fuzziness parameter $1/r$.

Measuring the RMS amplitude of the energy oscillations in both the pure-particle and pure-FDM simulations, we yield two similar plots for both scenarios, seen in Figure 7; the RMS amplitude as a function of number of particles N , and as a function of the reciprocal fuzziness parameter $1/r$.

We can fit these data sets with invertible elementary curves:

$$f(N) = \frac{a}{\sqrt{N}} \quad (34)$$

$$g(1/r) = \frac{b}{(1/r)^c} \quad (35)$$

Here f is the fit for the particle data, and g is the fit for the FDM data. The values for fitting parameters, $a \approx 9.84 \times 10^{-4}$, $b \approx 0.945$ and $c \approx 1.64$ come directly from Figure 7. Uncertainties are $\sigma_a \approx 6.51 \times 10^{-5}$, $\sigma_b \approx 0.61$

and $\sigma_c \approx 0.11$.

For a fixed RMS amplitude of oscillation, there must exist N and r such that the equality $f(N) = g(1/r)$ holds. Rearranging this equality yields an empirical power law for the effective number of quasi-particles in the FDM:

$$N_{\text{eff}}(r) = \alpha \left(\frac{1}{r} \right)^\beta \quad (36)$$

where $\alpha = \left(\frac{a}{b} \right)^2 \approx 0.1 \times 10^{-6} \pm 0.1 \times 10^{-6}$ and $\beta = 2c \approx 3.3 \pm 0.2$. For example, a fuzziness of $r \approx 0.00099$, as seen in the sample in IV B, yields an effective number of quasi-particles ~ 10000 . The higher level of relative error in the parameter b is slightly problematic. Nonetheless, the power law is compelling, and yields an effective quasi-particle mass:

$$m_{\text{eff}} = \frac{M}{\alpha} r^\beta \quad (37)$$

where M is the total mass of the system.

V. DYNAMICAL HEATING

Dynamical heating, or two-body relaxation, is a well documented phenomenon in stellar and galactic dynamics [6]. In a galaxy or star cluster, small stars passing by a larger, more massive star, experience an increase in velocity; large stars will experience dynamical friction passing through a field of smaller stars due to their collective gravity. Thus lighter particles will speed up, attaining a higher orbit and a higher potential energy, while the opposite is true for heavy particles.

The quasi-particle hypothesis suggests that an FDM halo will have the same interaction with a field of massive particles, or stars. In fact, this is the exact argument seen in [8].

Our goal in this section is to test the quasi-particle hypothesis through dynamical heating. In a similar fashion to section IV, we run many simulations and in two regimes: (VA) a purely particle system comprised of a heavy particle half and a light particle half, and (VB) a mixed FDM + particles system. In both cases, each component makes up half the total mass. By varying the ratio of heavy to light particle mass in the former, and the fuzziness parameter in the latter, we attempt to retrieve an empirical law for the effective mass of the FDM quasi-particles, seen in V C.

A. Mixed Particles

Classical dynamical heating occurs when there is variability in particle mass. The simplest test system for this phenomenon is comprised of two kinds of particles: heavy particles and light particles.

We want to set this up from equilibrium and watch as the system changes. So, we start with N_p particles whose phase-space coordinates (x_i, v_i) are sampled from the lowered Spitzer distribution, and total mass sums to M . We then choose the number of heavy particles $N_{\text{heavy}} < N_p$, and construct two new particle masses by:

$$\begin{cases} m_{\text{heavy}} = \frac{M}{2} \frac{1}{N_{\text{heavy}}} \\ m_{\text{light}} = \frac{M}{2} \frac{1}{N_{\text{light}}} \end{cases} \quad (38)$$

where $N_{\text{light}} = N_p - N_{\text{heavy}}$. To reassign masses to our already-sampled particles, we randomly sample N_{heavy} indices $j \in \{1, \dots, N_p\}$ without repetition, and reassign to each coordinate (x_j, v_j) a mass m_{heavy} . The rest of the particles/coordinates get a mass m_{light} . By this process, the total mass of the system remains unchanged, while half the mass is comprised of light particles, and the other half by heavy particles.

With this set-up for the initial conditions of our mixed particle system, we proceed by running simulations of 50000 particles for 256 collapse times, and for various heavy:light mass ratios, which we define as:

$$\mu = \frac{m_{\text{heavy}}}{m_{\text{light}}} \quad (39)$$

As can be seen in the example (with $\mu = 499$) of Figure 8, both the heavy component and light component maintain a “quasi-equilibrium” with $K/|W|$ maintained around the virial ratio $1/2$. Further, the dynamical heating we expect is observed. More such curves can be seen in Figure 10, and will be discussed further in V C.

A scatter plot of $\Delta E/E_i$ vs E_i for this example can be seen in Figure 4. We see that heating is more pronounced for particles whose initial energy is on the lower end. This trend is characteristic of all such plots. Overall, the heating increases with increasing μ , and goes to zero when $\mu \rightarrow 0$, as expected.

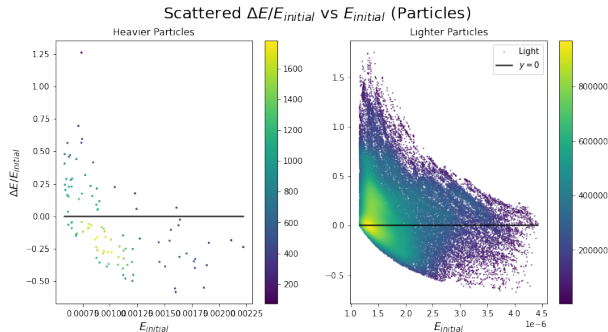


FIG. 4: The fractional change in energy $\Delta E/E_{\text{initial}}$ vs initial energy is plotted for every particle in the mixed mass particle system, for $\mu = 499$. On the left and right sides are heavy and light particles, respectively.

B. FDM and Particles

The quasi-particle hypothesis suggests that the density perturbations $\delta\rho_{\text{FDM}}$ in FDM perform the role of the heavy particles from the previous subsection V A. We thus set this system up as 50% FDM and 50% particles, by mass, both sampled from the lowered Spitzer distribution. In every simulation, there are 50000 particles, while the FDM fuzziness r is varied.

We present analogous energy and scatter plots to those seen in V A, seen in Figures 5 and 9, and observe the same qualitative behaviour as in the mixed particle regime. This example is for a fuzziness value of $r \approx 0.001981$. More energy plots can be seen in Figure 12, for varying r , and will be discussed in the following subsection.

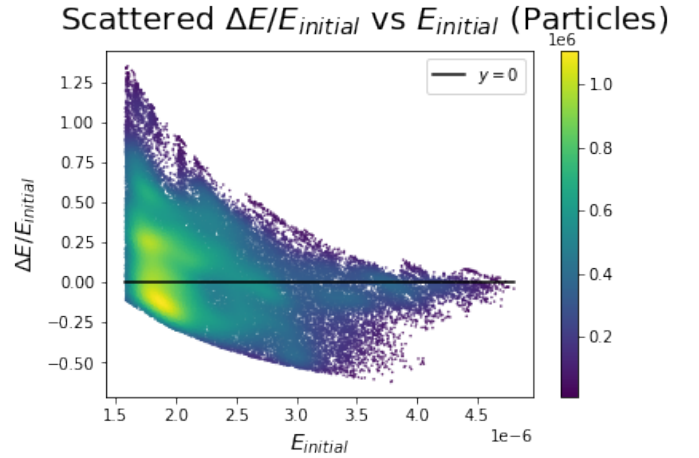


FIG. 5: The fractional change in energy $\Delta E/E_{\text{initial}}$ vs initial energy is plotted for every particle in the combined FDM+particle system.

C. Correspondence

Again, just as we saw in section IV, the similarities in the two regimes are remarkable. The distributions in Figures 4 and 5 are nearly identical. In both cases we see that while the (light) particles are heated and the other component is cooled, the system maintains a quasi-equilibrium, with $K/|W| \sim 1/2$ hovering around the virial ratio. In Figure 6 we also see that in both cases, the initial and final energy distributions follow a similar change, corresponding to heating of initially low-energy particles.

Moreover, we see that the transfer of energy from the FDM/Heavy component to the (light) particles increases with μ and r (see Figures 10 and 12 in appendix C). This suggests that there is a one-to-one correspondence between the mass ratio μ and the fuzziness parameter r . We attempt to find this relation via an empirical analysis.

In the figures just mentioned (10 and 12) we plot

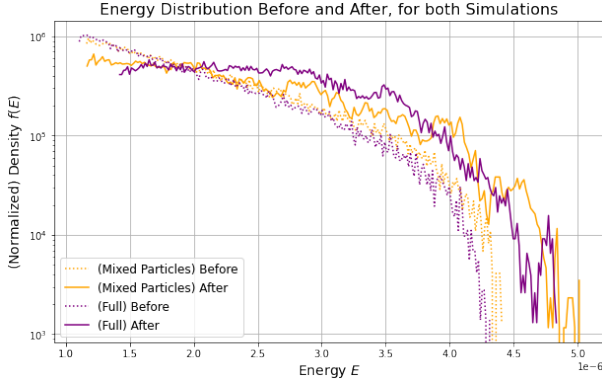


FIG. 6: From the two regimes in V A (purple) and V B (orange), we plot the distribution of energies for the (light) particle components, before (dotted) and after (solid).

the fractional change in total energy over time for the mixed mass particle and FDM+particle simulations, respectively. We arrive at a simple fitting formula for both sets of data:

$$\frac{\Delta E}{E_i}(t; \mu) = a_\mu (\ln(t+1))^{b_\mu} \quad (40)$$

$$\frac{\Delta E}{E_i}(t; r) = c_r (\ln(t+1))^{d_r} \quad (41)$$

Note that $E_i \equiv E(t=0)$ denotes the initial energy, and $\Delta E(t) = E(t) - E_i$. The formula has implicit dependence on the mass ratio μ and fuzziness r through the fitting parameters a, b and c, d , which in either case we presume to have explicitly either a μ - or r -dependence (e.g $d_r \equiv d(r)$).

The relation between μ and r is realized by the equality of equations (40) and (41). That is, for any fixed $\mu \in \mathbb{R}_{>0}$, there exists a corresponding $r \in \mathbb{R}_{>0}$ such that

$$\frac{\Delta E}{E_i}(t; \mu) = \frac{\Delta E}{E_i}(t; r), \quad \forall t > 0. \quad (42)$$

As a_μ, b_μ and c_r, d_r are fixed, and t varies, this equality holds if and only if:

$$a_\mu = c_r \text{ and } b_\mu = d_r \quad (43)$$

We set out to solve these equations using further empirical formula for the functions a and b . In Figures 11 and 13, we plot the corresponding fitting parameters for different values of μ and r , and use a crude linear fit for each:

$$a(\mu) = m_a \mu + y_a \quad (44)$$

$$b(\mu) = m_b \mu + y_b \quad (45)$$

$$c(r) = m_c r + y_c \quad (46)$$

$$d(r) = m_d r + y_d \quad (47)$$

This leaves us with some level of redundancy, as we arrive at two solutions for equations (43):

$$\begin{cases} \mu = \frac{m_c}{m_a} r + \frac{y_c - y_a}{m_a} \\ \mu = \frac{m_d}{m_b} r + \frac{y_d - y_b}{m_b} \end{cases} \quad (48)$$

We should find that these two agree, to within reasonable uncertainty. Moreover, we should expect that the terms $\frac{y_c - y_a}{m_a}$ and $\frac{y_d - y_b}{m_b}$ are close to zero, as this would agree with the idea that in the limit of small $r \rightarrow 0$, the mass of the quasi particles is also small $m_{\text{eff}} \rightarrow 0$.

From our current data, we find $m_a \approx 9.02 \times 10^{-6}$, $m_b \approx -1.15 \times 10^{-3}$, $y_a \approx -1.69 \times 10^{-4}$, $y_b \approx 3.16$, and $m_c \approx 27.2$, $m_d \approx -495$, $y_c \approx -6.44 \times 10^{-3}$, $y_d \approx 2.61$. This yields solutions:

$$\begin{cases} \frac{m_c}{m_a} \approx 3.02 \times 10^6 \text{ and } \frac{y_c - y_a}{m_a} \approx -695 \\ \frac{m_d}{m_b} \approx 4.30 \times 10^5 \text{ and } \frac{y_d - y_b}{m_b} \approx 478 \end{cases} \quad (49)$$

This large discrepancy may be due to multiple factors: (1) The likelihood function for our parameter estimators has two or more local maxima, (2) There is too little data, (3) We have the wrong fitting formula. In fact, our fitting formula was merely a guess without a phenomenological justification. It is likely that following arguments such as in [7], one arrives at a theoretical model for the energy transfer.

VI. DISCUSSION

We have quite nearly arrived at a computational verification of the quasi-particle hypothesis, in one spacial dimension. It is difficult to deny that, qualitatively, our tests suggest identical behaviour between each of the pairs of regimes. A quick analysis of the data from the first test gave us a simple one-to-one correspondence of fuzziness r and number of particles in the system (equivalently the effective particle mass). However, while the result from the second test is visually compelling, it remains less reliable. More data, a different fitting formula, or an all together different technique for numerical analysis may be necessary; this is a topic for future work.

There are other successes to mention as well, mainly improvements made since the midyear report. Numerous bugs in the code, regarding dynamics and energy conservation, have been ironed out, computational speed has greatly increased, and the code is fully capable of starting from our specified equilibrium conditions. The last of these is most important, an upgrade which has allowed for a more rigorous study of dynamical heating.

Another point to discuss is the accuracy of our analogous particle system representing the FDM quasi-particles in V A. Though the set-up may seem convincing, given that it yields a very similar behaviour to our FDM+particle simulation, the approach is actually somewhat naïve. As mentioned in the introduction, the formal quasi-particle hypothesis states that the effective mass is

proportional to the local phase-space density. A suitable procedure to replace the current set-up may then be to randomly sample a sequence of N_{heavy} lowered-Spitzer distributed particles with coordinates (x_j, v_j) , then reassign the mass to $m_j = \varepsilon_x \varepsilon_v f(x_j, v_j)$, for some suitable particle “width” ε_x and “height” ε_v . This idea came relatively recently in the research process and thus due to time constraints, has been left for future work.

The progress of the research is so far highly suggestive of our desired result, the confirmation of the quasi-particle hypothesis. For a yet more convincing study, further improvements such as those already mentioned should be pursued. We do not doubt that such efforts will yield a more accurate result. Moreover, there are some related and separate research directions we believe may be worthwhile, presented in the following section.

VII. FUTURE DIRECTIONS

The aforementioned suggestions to acquire more data, a different fitting formula or technique for numerical analysis, as well as the modified mixed mass particle system, are all changes that may improve the accuracy and validity of our study. However, there are further directions for this research that may bring more insight into understanding the dynamical interaction between FDM and particles.

- **Characterize the Energy Transfer.** Besides our empirical fitting of the curves from section V, a model for energy transfer should come from theoretical foundations. In fact, as we have mentioned earlier, [7] derives diffusion coefficients. Do their formulae match our results?
- **Determine the target DF.** We would like to determine a good time-dependent model for the final distribution(s) seen in Figure 6. This may tell us more information about energy transfer.
- **An analogous 3D system.** It is possible that the obtained one-to-one relation between the FDM fuzziness r and effective number of quasi-particles holds in higher dimensions. In this case, one can imagine simulating a 3-dimensional particle system just as in V A, with a “heavy” particle component corresponding to an FDM halo. The same questions as in the above points apply, and further, a comparison of simulation results to real astrophysical observations is possible (e.g, data from the Segue 1 and 2 UFDs).

We (Professor Widrow and I, the author) plan to continue this research into the first 4-6 weeks of the spring/summer semester. The goal is an eventual publication.

ACKNOWLEDGEMENTS

I would like to thank my supervisor Prof. Larry Widrow for the project, as well as Queen’s University and the Arthur B. McDonald Institute for funding the initial stages of this research through the Research and Outreach Fellowship. I also acknowledge that extensive use of the NumPy, SciPy and Matplotlib packages for Python3 was fundamental in the development of our simulations.

Appendix A: Details on Numerical Techniques

Particle-Mesh codes may not be familiar to all readers, so this appendix serves to define further details of the numerical techniques, as well as how we implemented them in Python3. We also describe some of the other capabilities of our code.

1. Initial Setup

In every case, the system is setup on a grid of N linearly spaced points:

$$x = [x_0, x_1, x_2, \dots, x_{N-1}] \quad (\text{A1})$$

(indexing starts with $i = 0$ in Python3). These values serve as edges for histogramming positions of particles, and positions at which the density, potential and acceleration fields are defined. The width of the bins is the constant

$$dx = x_{i+1} - x_i$$

The choice of N will determine the accuracy of the FFT Poisson Solver described below; a higher value N will both increase the accuracy, and increase the computational cost. In IIID, we described how to get the minimal N in the case that FDM is present.

In any given simulation, we further define the box width L , and apply the boundaries:

$$x_0 = -L/2 \quad (\text{A2})$$

$$x_{N-1} = L/2 \quad (\text{A3})$$

2. Calculating Density

At any given time step of a simulation, it is necessary to calculate the acceleration field defined on the grid. To do this, density must be calculated first. It is straightforward to calculate the FDM density: $\rho_{\text{FDM}} = m_{\text{FDM}} |\psi|^2$.

Calculating particle density amounts to histogramming the positions of particles. Naturally, we histogram using bins of length equal to the mesh-size dx . The particle density in a given bin is then:

$$\rho_k = \frac{n_k}{dx} \cdot \Sigma \quad (\text{A4})$$

where n_k is the number of particles counted in the k^{th} bin, and Σ is the mass per unit area defined for each particle. Note here that Σ must have the specified dimensions in the 1D scenario, as each particle is really treated as an infinite 2D sheet perpendicular to our grid z (see problem 4.21 in Binney & Tremaine [6]).

In practice it is necessary to interpolate the histogrammed values N_k from *between* the grid points x_0, x_1, \dots, x_{N-1} *onto* the grid points. We do this simply by taking an arbitrary array of length N :

$$\tilde{n} = [\tilde{n}_0, \tilde{n}_1, \dots, \tilde{n}_{N-1}]$$

and then for $i \in \{1, 2, \dots, N-2\}$, we let:

$$\tilde{n}_i = \frac{1}{2}(n_{i-1} + n_{i+1})$$

and for $i = 0, N-1$:

$$\begin{aligned}\tilde{n}_0 &= \frac{1}{2}(n_{N-1} + n_1) \\ \tilde{n}_{N-1} &= \frac{1}{2}(n_{N-2} + n_0)\end{aligned}$$

We then re-assign $\forall k \in \{0, \dots, N-1\}$:

$$n_k \leftarrow \tilde{n}_k$$

Note that in the case of periodic boundary conditions, the last step, for $i = 0, N-1$, preserves them. If the box isn't periodic, and instead isolated, one would expect this to be problematic. However, with a large enough box size, no particles ever reach the edge in our simulations, so the issue is avoided.

3. Calculating Potential

The second main ingredient in evolving the system is knowing the gravitational potential Φ . We must solve for Φ from Poisson's Equation in Eq(8), and we do so using a Fast-Fourier-Transform (FFT) method. As seen in III, we do this in both:

- Isolated boundary conditions.
- Periodic boundary conditions.

the latter of which we have reserved to describe here.

a. Periodic BCs

The basic idea is that applying the Discrete-Discrete Fourier Transform (since we're in a periodic box with a discrete signal/sequence) on Poisson's equation yields:

$$\frac{\partial^2}{\partial x^2} \left(\sum_{n=0}^{N-1} \hat{\Phi}(k_n) e^{ik_n x} \right) = 4\pi \left(\sum_{n=0}^{N-1} \hat{\rho}(k_n) e^{ik_n x} - \langle \rho \rangle \right)$$

where $k_n \equiv 2\pi n/L$, L being the length of the box. Notice that $\langle \rho \rangle = \hat{\rho}(k_0)$, so that from the above equation we get:

$$\begin{cases} -k_n^2 \hat{\Phi}(k_n) = 4\pi \hat{\rho}(k_n), \forall n \\ 0 \cdot \hat{\Phi}(0) = 0 \end{cases}$$

yielding Poisson's equation fully solvable on our 1D mesh by simply applying an FFT to the density and applying an IFFT to the Fourier coefficients of the potential, defined by:

$$\begin{cases} \hat{\Phi}(k_n) = -\frac{4\pi}{k_n^2} \cdot \hat{\rho}(k_n) \quad \forall n \\ \hat{\Phi}(0) = 0 \end{cases}$$

4. Initial Conditions

Our code can simulate two distinct initial conditions (ICs): a stationary collapse, and an equilibrium model. The latter was already described in III A.

a. Stationary Gaussian

To begin with an initial collapse, we set up FDM and particle distributions under a Gaussian density:

$$\rho_{\text{FDM/part}}(x) = \frac{M_{\text{FDM/part}}}{\sqrt{2\pi\sigma_x^2}} e^{-x^2/2\sigma_x^2} \quad (\text{A5})$$

where we choose the standard deviation σ_x in x .

To set up the FDM under this density, but as a stationary wave, is straightforward. Following the identity $\rho \equiv m|\psi|^2$:

$$\psi(x) = \sqrt{\rho(x)/m_{\text{FDM}}} \quad (\text{A6})$$

In the case of the particles, we simply randomly sample a normalized Gaussian distribution².

5. Computational Complexity

Here we evaluate the approximate number of arithmetic/computational operations required for one time-step Δt of evolving the FDM. The algorithm breaks down as follows:

1. KICK: 1D-array multiplication $\sim N$
2. DRIFT:
 - (a) FFT: $\sim N \log N$

² This can be done using built in NumPy functions, in Python3.

(b) Multiplication (by $e^{ir\Delta tk^2}$) $\sim N$

(c) IFFT: $\sim N \log N$

3. UPDATE POTENTIAL (doubled grid)

(a) FFT: $\sim 2N \log(2N)$

(b) Multiplication $\hat{G}_k \hat{\rho}_k$: $\sim 2N$

(c) IFFT: $\sim 2N \log(2N)$

4. KICK: $\sim N$

Altogether, the total number of operations per time-step is:

$$N(5 + 4 \log 2) + 6N \log N \quad (\text{A7})$$

Appendix B: Virial Equation in 1D

About halfway through the research process, we came to question whether the virial equation is the same in 1D gravitation as in 3D. As it happens, it is. In this appendix we show the key change to the derivation of the tensor virial equation than that seen in Binney&Tremaine ([6, 4.8.3]):

$$\frac{1}{2} \frac{d^2 I_{jk}}{dt^2} = 2K_{jk} + W_{jk} \quad (\text{B1})$$

that is necessary to obtain the same result 1D.

The only change is the definition of the Chandrasekhar potential energy tensor. In [6], potential tensor is defined Φ_{ij} in 3D. We must define it in 1D analogously using the 1D Green's function for Poisson's equation (which is $\frac{|x|}{2}$). I will continue to use the index/vector/tensor notation even though this is in 1D.

$$\Phi_{ij} \equiv \frac{1}{2} \int d^1 \vec{x}' \left[\rho(x') \frac{(x_i - x'_i)(x_j - x'_j)}{|\vec{x} - \vec{x}'|} \right] \quad (\text{B2})$$

It should be clear that this gives $\Phi_{ii} = \frac{1}{2} \int |x - x'| \rho(x') dx' = \Phi(x)$. Continuing on, define the potential energy tensor and do some calculations:

$$\begin{aligned} W_{ij} &\equiv \frac{1}{2} \int d^1 \vec{x} [\rho \Phi_{ij}] \\ &= \frac{1}{4} \int \int \rho(x) \rho(x') \frac{(x_i - x'_i)(x_j - x'_j)}{|\vec{x} - \vec{x}'|} dx' dx \\ &= \frac{1}{4} \left[\int \int \rho(x) \rho(x') \frac{x_i(x_j - x'_j)}{|\vec{x} - \vec{x}'|} dx' dx \right. \\ &\quad \left. - \int \int \rho(x) \rho(x') \frac{x'_i(x_j - x'_j)}{|\vec{x} - \vec{x}'|} dx dx' \right] \\ &= \frac{1}{4} \int \rho(x) x_i \left[2 \int \rho(x') \frac{(x_j - x'_j)}{|\vec{x} - \vec{x}'|} dx' \right] dx \\ &= \frac{1}{2} \int \rho(x) x_i \left[\int \rho(x') \frac{(x_j - x'_j)}{|\vec{x} - \vec{x}'|} dx' \right] dx \quad (\text{B3}) \end{aligned}$$

Now observe:

$$\begin{aligned} \frac{\partial \Phi}{\partial x_j} &= \frac{1}{2} \int dx' \frac{\partial |x - x'|}{\partial x_j} \rho(x') \\ &= \frac{1}{2} \int dx' \left[\frac{\partial}{\partial x_j} \left(\sum_k (x_k - x'_k)^2 \right)^{1/2} \right] \rho(x') \\ &= \frac{1}{2} \int dx' \left[\frac{1}{2} \left(\sum_k (x_k - x'_k)^2 \right)^{-1/2} \right. \\ &\quad \left. \times \frac{\partial}{\partial x_j} \left(\sum_k (x_k - x'_k)^2 \right) \right] \rho(x') \\ &= \frac{1}{2} \int dx' \left[\frac{1}{2|x - x'|} \sum_k 2(x_k - x'_k) \delta_{jk} \right] \rho(x') \\ &= \frac{1}{2} \int dx' \frac{1}{|x - x'|} (x_j - x'_j) \rho(x') \\ &= \frac{1}{2} \int \rho(x') \frac{(x_j - x'_j)}{|x - x'|} dx' \quad (\text{B4}) \end{aligned}$$

The important result:

$$\Rightarrow \int \rho(x') \frac{(x_j - x'_j)}{|x - x'|} dx' = 2 \frac{\partial \Phi}{\partial x_j} \quad (\text{B5})$$

Plugging this last bit into (B3), we get:

$$W_{ij} = \int \rho(x) x_i \frac{\partial \Phi}{\partial x_j} dx \quad (\text{B6})$$

Which is exactly the same as in the 3D case. The final result, equation (B1), then follows in the same way as seen in Binney & Tremaine.

Now when a system is virialized, the moment of inertia will be constant, so:

$$\frac{d^2 \mathbf{I}}{dt^2} = 0 \iff 2K + W = 0 \quad (\text{B7})$$

This yields the virial ratio desired.

Appendix C: Figures

Some large figures referenced in the main body of the document are placed in the following pages.

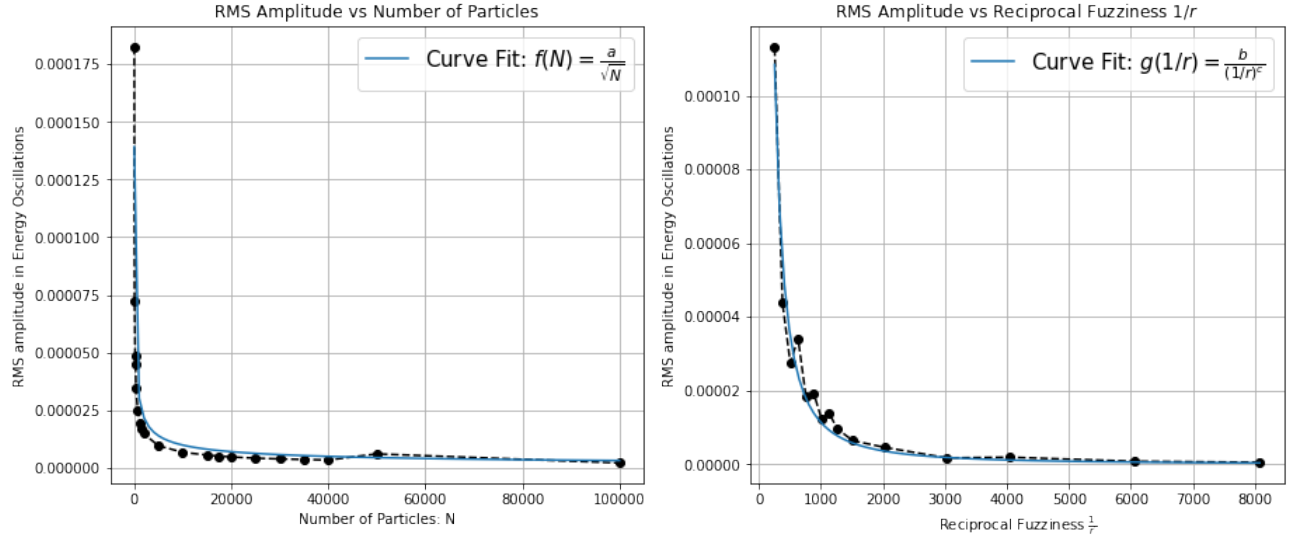


FIG. 7: RMS amplitudes of oscillation in total energy for varying particle numbers and fuzziness parameters, along with curve fits for the data. For the fit on the left: $a = 0.0009844419002455697$. For the fit on the right: $b = 0.9447031$ and $c = 1.64030959$.

Variation from Mean Total Energies in Particles over Time

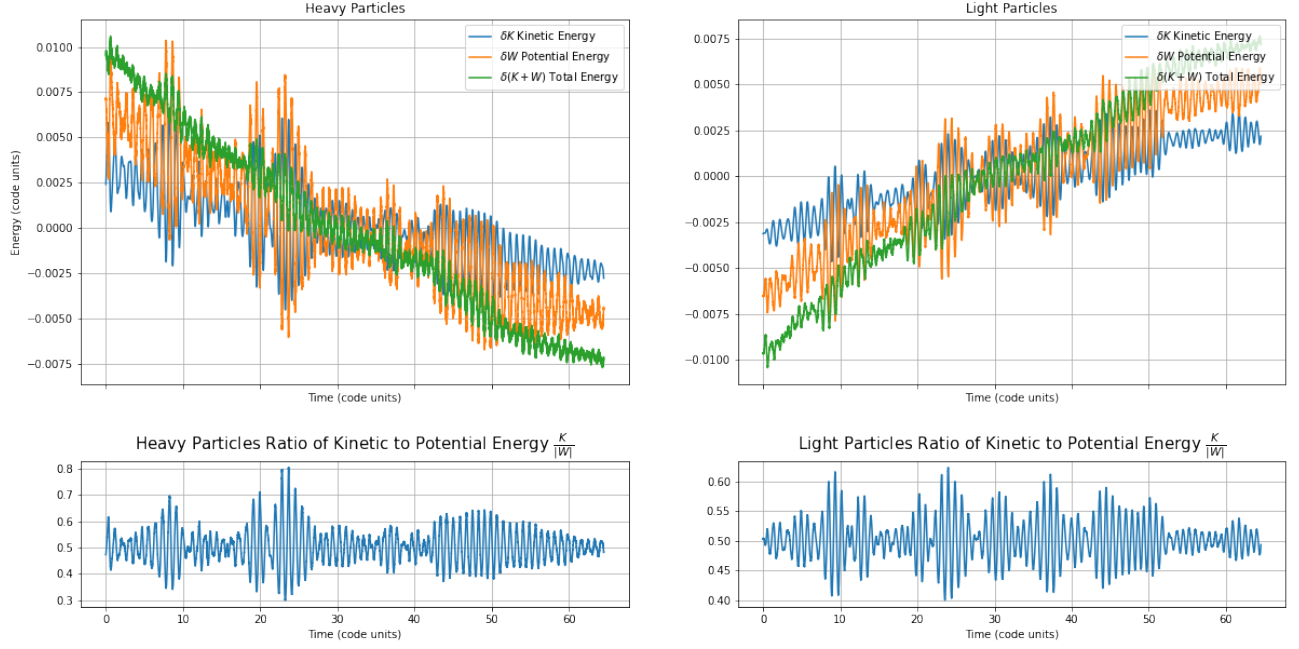


FIG. 8: Difference from mean energies are plotted ($\delta E \equiv E - \langle E \rangle$), along with kinetic:potential energy ratios, for the mixed particle simulation in V A. Left and right sides are for heavy and light particles, respectively.

Variation from Mean Total Energies in Particles over Time

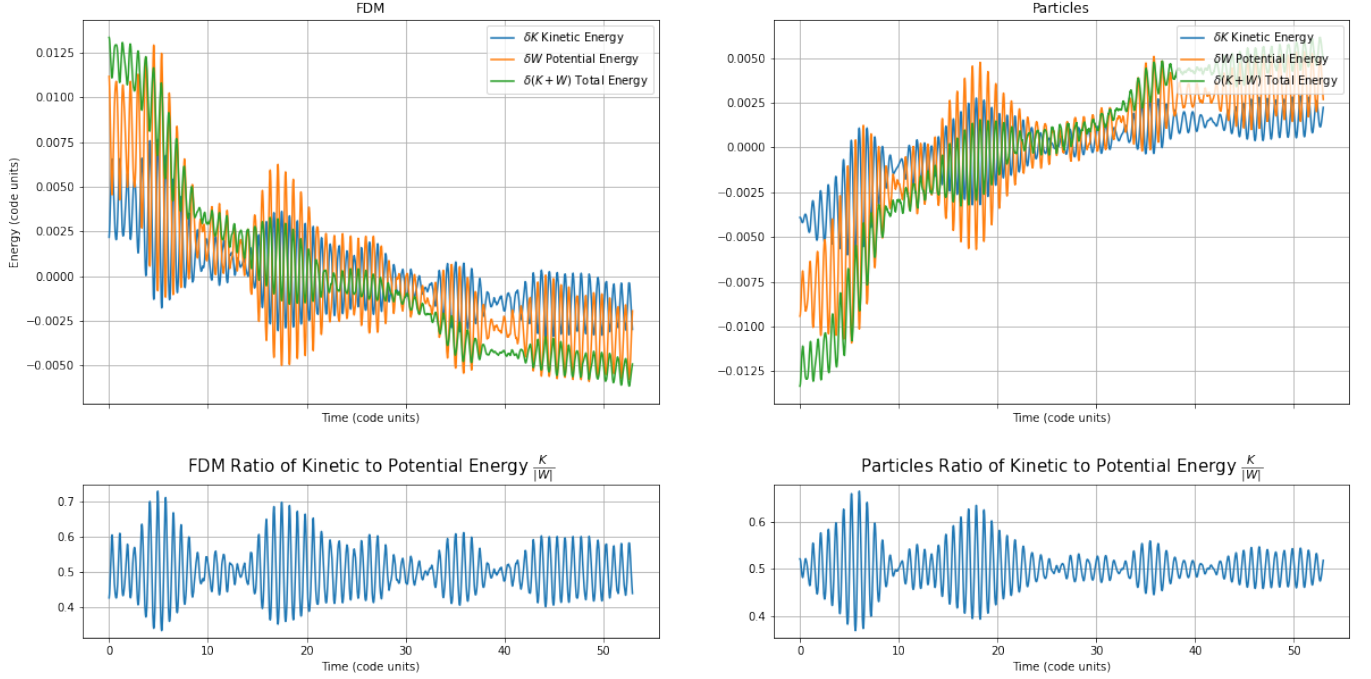


FIG. 9: Difference from mean energies are plotted ($\delta E \equiv E - \langle E \rangle$), along with kinetic:potential energy ratios, for the mixed particle simulation in V B. Left and right sides are for FDM and particles, respectively.

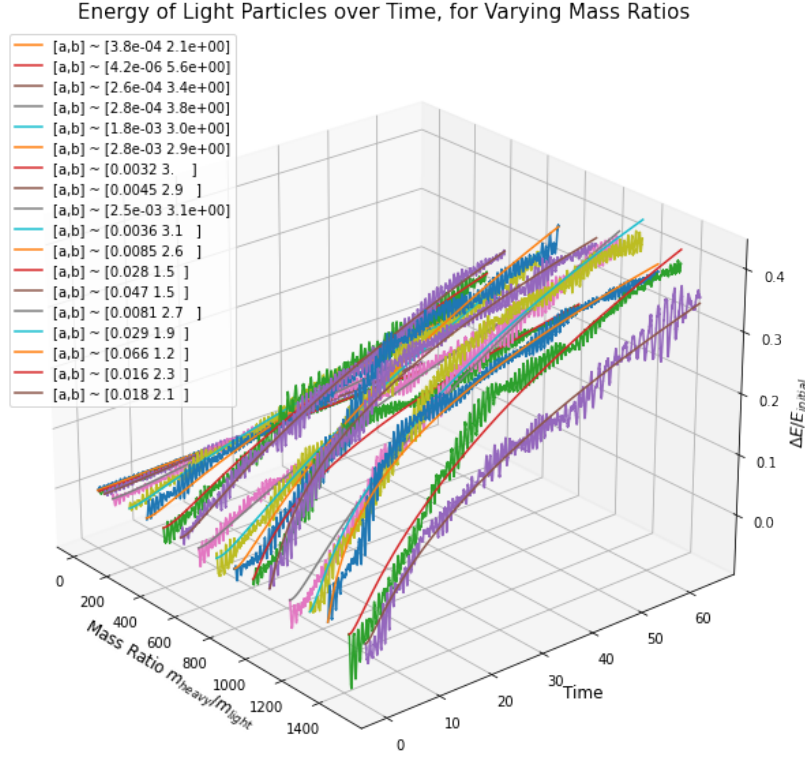


FIG. 10: Energy transfer curves from the mixed particle simulations, for varying mass ratio μ . Parameters for the curve fit described are seen in the legend.

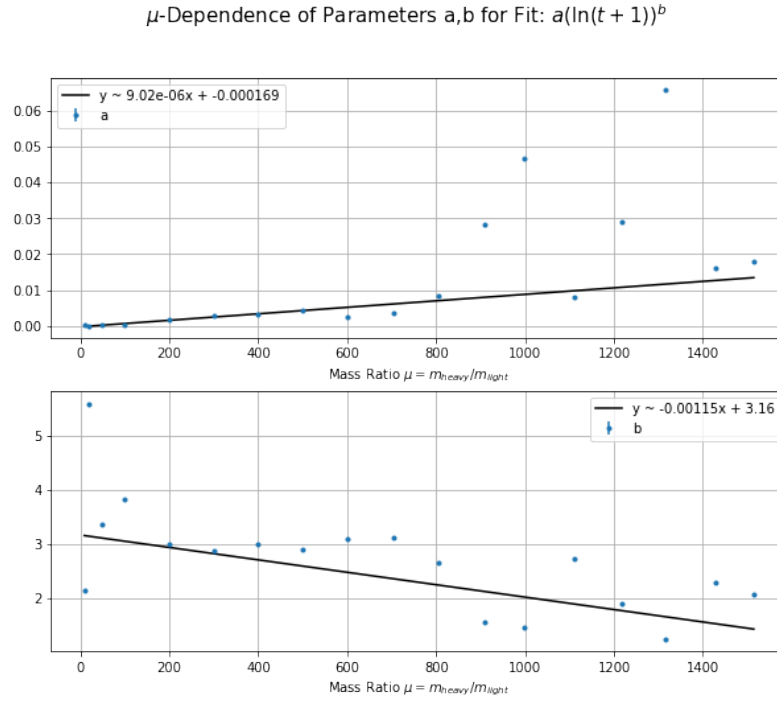


FIG. 11: The parameters for each curve fit in Figure 10 are plotted against the corresponding simulation's μ value. We attempt to fit both sets of data.

Fractional Energy Change $\Delta E/E_{\text{initial}}$ of Particles over Time, for Fuzziness Parameters

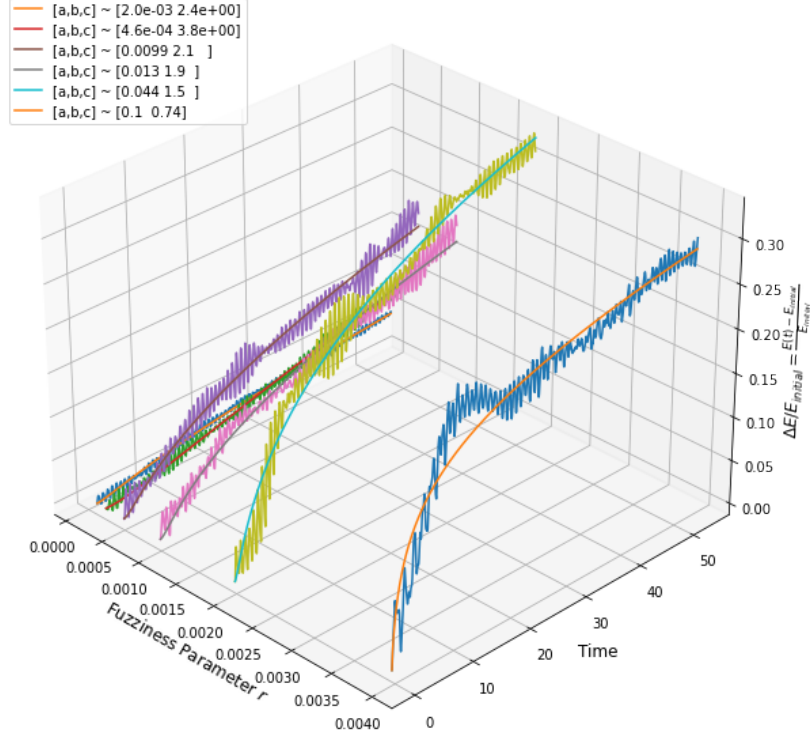


FIG. 12: Energy transfer curves from the FDM+particle simulations, for varying fuzziness r . Parameters for the curve fit described are seen in the legend.

r -Dependence of Parameters a, b for Fit: $a(\ln(t+1))^b$

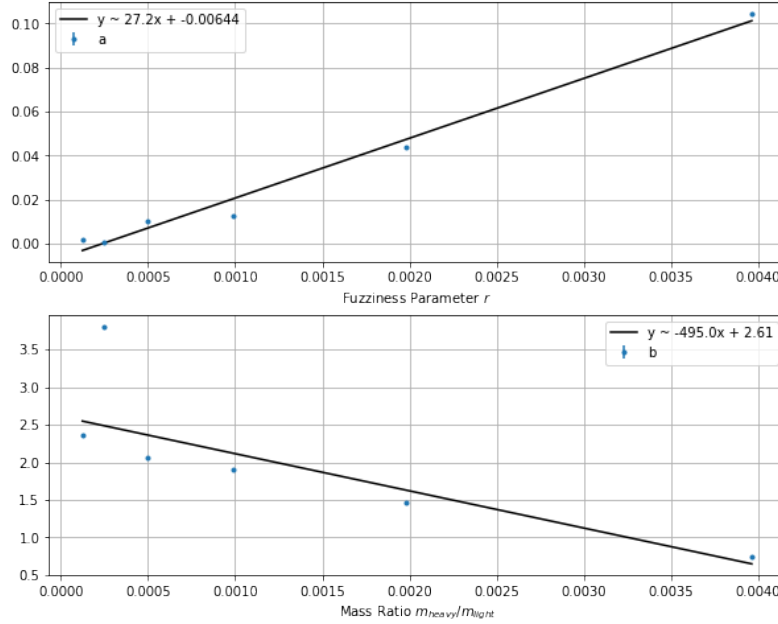


FIG. 13: The parameters for each curve fit in Figure 12 are plotted against the corresponding simulation's r value. We attempt to fit both sets of data with a linear function.

-
- [1] D. H. Weinberg, J. S. Bullock, F. Governato, R. K. de Naray, and A. H. G. Peter, Cold dark matter: Controversies on small scales, *Proceedings of the National Academy of Sciences* **112**, 12249 (2015).
 - [2] A. Klypin, A. V. Kravtsov, O. Valenzuela, and F. Prada, Where are the missing galactic satellites?, *The Astrophysical Journal* **522**, 82 (1999).
 - [3] S. May and V. Springel, Structure formation in large-volume cosmological simulations of fuzzy dark matter: impact of the non-linear dynamics, *Monthly Notices of the Royal Astronomical Society* **506**, 2603 (2021).
 - [4] L. Hui, J. P. Ostriker, S. Tremaine, and E. Witten, Ultralight scalars as cosmological dark matter, *Physical Review D* **95**, 10.1103/physrevd.95.043541 (2017).
 - [5] L. Hui, Wave dark matter, *Annual Review of Astronomy and Astrophysics* **59**, 247 (2021).
 - [6] J. Binney and S. Tremaine, *Galactic Dynamics: Second Edition* (2008).
 - [7] B. Bar-Or, J.-B. Fouvry, and S. Tremaine, Relaxation in a fuzzy dark matter halo. II. self-consistent kinetic equations, *The Astrophysical Journal* **915**, 27 (2021).
 - [8] N. Dalal and A. Kravtsov, Not so fuzzy: excluding fdm with sizes and stellar kinematics of ultra-faint dwarf galaxies (2022).
 - [9] N. Dalal, J. Bovy, L. Hui, and X. Li, Don't cross the streams: caustics from fuzzy dark matter, *Journal of Cosmology and Astroparticle Physics* **2021** (03), 076.
 - [10] F. Edwards, E. Kendall, S. Hotchkiss, and R. Easther, PyUltraLight: a pseudo-spectral solver for ultralight dark matter dynamics, *Journal of Cosmology and Astroparticle Physics* **2018** (10), 027.
 - [11] L. M. Widrow and N. Kaiser, Using the Schroedinger Equation to Simulate Collisionless Matter, **416**, L71 (1993).
 - [12] R. Hockney and J. Eastwood, *Computer Simulation Using Particles* (CRC Press, 2021).
 - [13] G. Casella, C. P. Robert, and M. T. Wells, Generalized accept-reject sampling schemes, in *A festschrift for Herman Rubin*, IMS Lecture Notes Monogr. Ser., Vol. 45 (Inst. Math. Statist., Beachwood, OH, 2004) pp. 342–347.
 - [14] L. C. Andrews, *Special functions of mathematics for engineers*, 2nd ed. (SPIE Optical Engineering Press, Bellingham, WA; Oxford University Press, Oxford, 1998) pp. xx+480.
 - [15] W. Kutta, Beitrag zur näherungsweise Integration totaler Differentialgleichungen, *Zeit. Math. Phys.* **46**, 435 (1901).
 - [16] J. Eastwood and D. Brownrigg, Remarks on the solution of poisson's equation for isolated systems, *Journal of Computational Physics* **32**, 24 (1979).
 - [17] R. Courant, K. Friedrichs, and H. Lewy, Über die partiellen Differenzengleichungen der mathematischen Physik, *Mathematische Annalen* **100**, 32 (1928).
 - [18] L. M. Widrow and G. Bonner, Vertical oscillations of fluid and stellar discs, *Monthly Notices of the Royal Astronomical Society* **450**, 266 (2015).